A comparative study on the performance of binary SnO₂/NiO/C and Sn/C composite nanofibers as alternative anode materials for lithium ion batteries

Victor A. Agubra, Luis Zuniga, David Flores, Howard Campos, Jahaziel Villarreal, Mataz Alcoutlabi*

Department of Mechanical Engineering, University of Texas, Rio Grande Valley, Edinburg, TX 78539, United States

ABSTRACT

The development of alternative anode materials out of flexible composite nanofibers has seen a growing interest. In this paper, binary carbon nanofiber electrodes of SnO₂/NiO and Sn nanoparticles are produced using a scalable technique, Forcespinning (FS), and subsequent thermal treatment (carbonization). The Sn/C composite nanofibers were porous and flexible, while the SnO₂/NiO composite nanofibers had "hairy-like" particles and pores on the fiber strands. The nanofiber preparation process involved the FS of Sn/PAN and SnO₂/NiO/PAN solution precursors into nanofibers and subsequent stabilization in air at 280°C and calcination at 800°C under an inert atmosphere. The flexible composite nanofibers were directly used as working electrodes in lithium-ion batteries without a current collector, conducting additives, or binder. The electrochemical performance of the SnO₂/NiO/C and Sn/C composite fiber anodes showed a comparable cycle performance of about 675 mAhg⁻¹ after 100 cycles. However, the SnO₂/NiO/C electrode exhibited a better rate performance than the Sn/C composite anode and was able to recover its capacity after charging with a higher current density. A postmortem analysis of the composite nanofiber electrode after the aging process revealed a heavily passivated electrode from the electrolyte decomposition by-products. The synthesis and processing methods used to produce these composite nanofibers clearly were a factor for the high rate capability and excellent cycle performance of these binary composite electrodes, largely on the account of the unique structure and properties of the composite nanofibers.

© 2016 Published by Elsevier Ltd.

1. Introduction

The use of nanostructured materials for energy storage devices has been the trend in recent years. Nanostructured fibers made from metals, metal oxides, ceramics, and composites have been developed for use in various energy storage devices. The popularity of these nanostructured fibrous materials stem from their many attributes: controllable fiber diameter, high surface area- to-volume ratio, low density, and high pore volume [1,2]. These properties make the nanofiber structure advantageous compared to their powder, crystal, nanowire, thin film, etc. counterparts [3,4], when used as electrodes in lithium ion batteries (LIB). These nano fibrous metal/metal oxides and ceramic composite electrodes deliver a comparable electrochemical performance including: a stable cycle performance, enhanced capacity, and superior low temperature performance [5,6]. These improved properties/ performances of composite nanofibers are often attributed to the non-woven structure that gives the nanofibers its high labyrinth-like porous structure, good high surface and interfacial areas resulting in a short-diffusion distance of Li-ions (Li⁺) during the charge/discharge cycles. These physical characteristics lead to the creation of more reactive sites while the porous structure provides the buffering effect to accommodate the large volume changes often associated with the alloying/de-alloying of lithium with these metal/metal oxide and ceramic composite compounds [7,8].

Tin (Sn)-based derivatives such as tin oxides, tin sulfides, and stannates have become attractive anode materials for LIBs [9–11].


The popularity of these Sn-based lithium alloys stem from their properties that include the ability to inhibit solvent co-intercalation and significant improvement in electrochemical performance over the commercial graphite anode in LIBs [12,13]. In addition, these Sn-based/carbon nanofiber composites are easy to process and exhibit a lower potential hysteresis compared to other transition metal oxides [14,15]. The crystal structure of Sn has the ability to host a higher amount of lithium ions, i.e. about four (4) atoms (i.e. Li_xSn, $0 < X \leq 4.4$) compared to carbonaceous anode (i.e. $LixC_6$, $0 < X \leq 1$) thereby giving Sn-based/C composite nanofibers a higher lithium storage capacity. Typically, the Sn-based/C nanofiber composite electrodes show a reversible capacity between $800\,mAhg^{-1}$ and $600\,mAhg^{-1}$ even at a higher current density of $200\,mAg^{-1}$–$1\,Ag^{-1}$ [8,16]. The electrochemical performance has been found to largely depend on the carbonization temperature which tends to have a direct impact on the fiber morphology, structure, and the pore distribution [8].

Ternary composites of Sn/CNFs containing other metals and their oxides have been investigated and shown to further improve the conductivity and the cyclic and rate performance of the composite electrode. Tin-based ternary composites such as SnO_2/ZnO heterogeneous nanofibers [17,18], Nitrogen doped CNFs with Sn quantum dots [19], Co-Sn alloy carbon nanofibers [20], and Fe_3O_4/SnO_2 coaxial nanofibers [21] have been reported to enhance the electrochemical performance when used as anodes in LIBs. For instance, the N-doped Sn/CNF's, provides fast and versatile electrolyte transport and can act as efficient electron transport pathways and stable mechanical supports to keep the structural integrity of the electrodes during cycling [19]. On the other hand, the Cobalt in Sn/CNFs reduces the volume expansion and enhances the electrical conductivity of the electrode [2]. In this paper, we compare the electrochemical performance of Sn-particles/carbon composite nanofibers with that of SnO_2/NiO binary carbon composite nanofibers. These composite nanofibers are considered potential alternative anodes for LIBs. The composite nanofibers were prepared using a facile technique known as Forcespinnning® (FS) that was recently developed at UTPA [22]. Several methods can be used to produce nanofibers such as electrospinning [23], liquid shearing method [24], centrifugal and/or rotary jet-spinning [25,26], electrospray [27], touch-brush spinning [28] and reactive magnetospinning [29]. The FS method is the trade name of the centrifugal spinning method that has been recently used to produce fibers for energy storage [30–34] and biomedical applications [35] .The centrifugal spinning process was originally
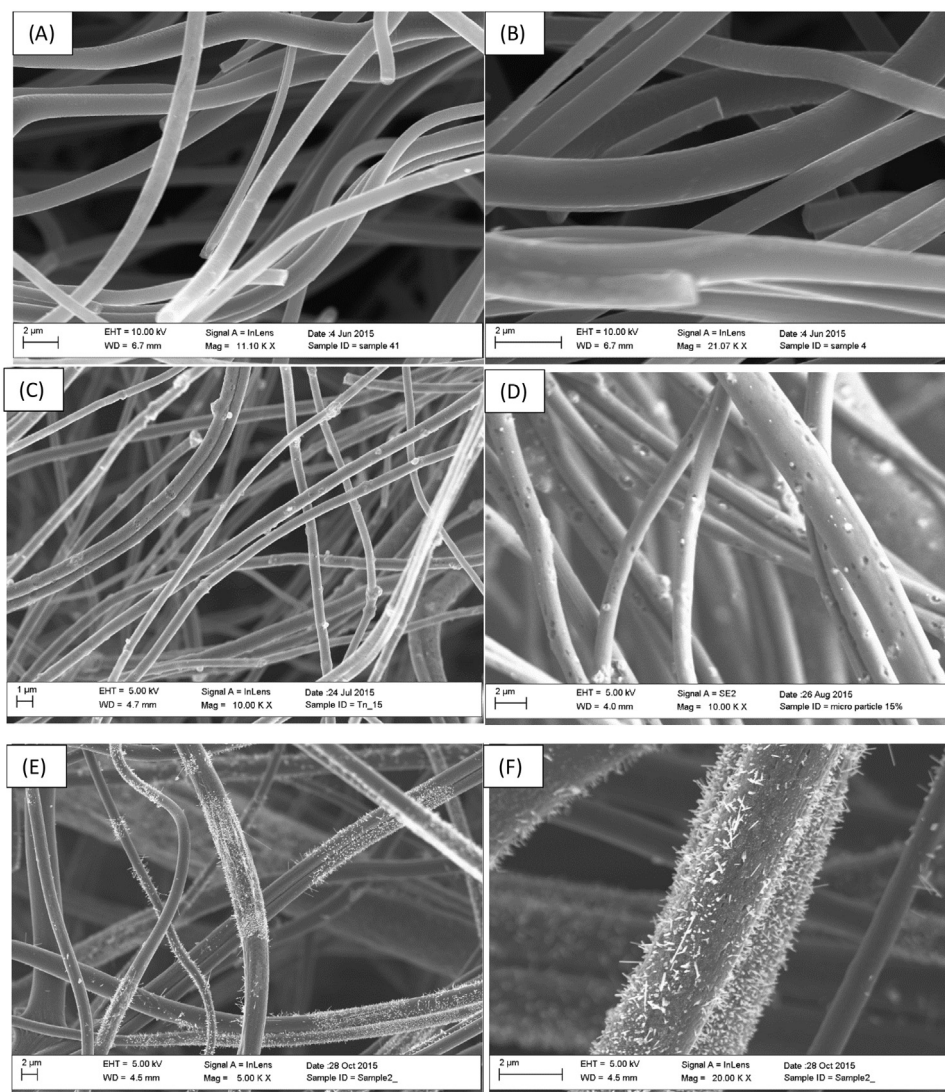
Fig. 1. SEM images of solid carbon fiber (a,b), Sn/CNFs composite fibers (c,d) with nanoparticles of the Sn sttached to the fibers strands and pores distributed evenly. SnO_2/NiO/CNFs composite fibers at different magnification showing unform fiber mat (e.f), and fiber strands with nanoparticles of the SnO_2 and NiO attached to the fibers strands in a hair-like structure with pores distributed evenly.

developed and used by Hopper in 1924 to produce artificial silk threads from viscose or equivalent substances by applying centrifugal forces to a viscous material [36] and was extensively used to produce fibers in nano/micro range [37]. The centrifugal spinning method has been recently used to produce polymer nanofibers after the pioneer work reported by Weitz et al. on the unexpected formation of nanofibers, with diameters in the nanometer range, from polymer solution using a standard spin-coating process [38]. This process was named as Nozzle-Free Centrifugal Spinning.

The FS method has several features such as: capability for dual material feed that allows continuous material feed, an almost 100% yield and solvent-free processing for melt spinning with melt temperatures up to 350 °C, and requires less solvent or no solvent at all, thereby making it a more cost effective method and better safety of operation compared to other nanofiber making techniques such as electrospinning, melt-blowing, and the in-house built centrifugal system [39]. In this paper, the FS method is used to produce Sn/PAN and SnO_2/NiO/PAN nanofibers from solution precursors. The collected fibrous mats were subjected to different thermal treatments to produce uniform and flexible Sn/C and SnO_2/NiO/C nanofibers with hairy-like morphology of the dispersed SnO_2/NiO particles on the porous fiber strands.

2. Experimental

2.1. Materials

Poly(acrylonitrile) with average Mw 150,000 used as the carbon precursor was purchased from Sigma Aldrich USA, while solvent N, N-dimethyl Formamide (DMF) was obtained from Fisher Scientific USA. The commercial lithium foil, lithium hexafluorophosphate ($LiPF_6$), ethylene carbonate (EC), dimethyl carbonate (DMC) were purchased from MTI corp. USA. A Whatman glass microfiber from GE healthcare was used as a separator. The nano powder (Sn, 99.9%, 60–80 nm) was purchased from US research Nanomaterials while that of the Tin (II) 2-ethylhexanoate and Nickel (II) acetate tetrahydrate (98%) were purchased from Sigma Aldrich USA and used as received.

2.2. The production of Sn/PAN and SnO_2/NiO/PAN fiber mats

The Sn/PAN nanofiber mats were prepared by adding 15 wt% of Tin (Sn) nanoparticles of the base polymer polyacrylonitrile (PAN) and dissolved in DMF. The DMF/Sn suspension was then sonicated in a water bath for 30 min to obtain a homogenous dispersion of Sn particles in the solvent. The base polymer, PAN (12 wt%) was then added to the DMF/Sn suspension and mechanically mixed using magnetic stirring for 24 h at room temperature. For the SnO_2/NiO/PAN precursor the weight percentages of the Tin (II) 2-ethyl-hexanoate and Nickel (II) acetate tetrahydrate were 15 wt% and 10 wt%, respectively, and for the baseline sample, the CNFs were forcespun from the PAN with concentration of 12 wt% of the solution (i.e. PAN/DMF). Forcespining was used to produce the nano fibrous mats from PAN, Sn/PAN and SnO_2/NiO/PAN solution precursors. A thin fiber spun-bond was used on a fan box as the substrate for the deposition of fibers. In the FS technique, centrifugal forces are used to extrude polymer solutions or melts through the spinneret. An amount of 2 mL of the precursor solution was injected into the needle-based spinneret equipped with 30 gauge half-inch regular bevel needles. The rotational speed of the spinneret was kept at 8000 rpm. The substrate was rotated 90° after each run and the needles were changed after each run. The Sn/PAN and SnO_2/NiO/PAN fibrous mats were removed from the substrate drum and dried at 120 °C under vacuum for 24 h prior to being carbonized. The forcespun nanofibers mats were then further stabilized in air at 280 °C for 5 h, and then calcined at 800 °C for 2 h in an argon atmosphere to obtain the Sn/Carbon and SnO_2/NiO/ carbon composite nanofiber mat (heating rate was 3 °C min^{-1}).

The structure, morphology, and elemental composition of the Sn/C and SnO_2/NiO/C composite nanofiber mats were analyzed using scanning transmission electron microscopy (STEM/EDAX) from Sigma VP Carl Zeiss. The crystal structure and the surface analysis were evaluated using X-ray powder diffraction and XPS from Bruker and Thermo Scientific, respectively. The thermal and residual weight of carbon in the Sn/PAN and SnO_2/NiO/PAN matrix was carried out using Thermo-Gravimetric analyzer (TGA) from TA Instruments (QA 600). The temperature was ramped up from 24 °C to 700 °C using a heating rate of 10 °C/min in nitrogen gas. The surface area, pore volume and pore size were evaluated from the Brunauer, Emmett and Teller (BET) analysis using micromeritics ASAP 2020. For the postmortem analysis of the aged electrode, the cell was discharged to 0.01 V and transferred into the glovebox. The cell was then disassembled and the harvested electrode was washed in DMC solvent and dried in vacuum.

2.3. Sn/C NFs and (SnO_2/NiO)/C half-cell assembly

Electrochemical experiments were performed using coin-type (2032) half cells containing Sn/C and SnO_2/NiO/C composite nanofibers as the working electrode. The cell preparation was performed in a glove box (Mbraun, USA) filled with high purity Argon with oxygen and moisture content <0.5 ppm. The Sn/C and SnO_2/NiO/C electrodes formed flexible free-standing nanofibers, which were punched directly and used as binder-free electrodes without any additives. The average electrode thickness was around 2 mm, and the average weight was in the range of 2–4 mg. Lithium metal was used as the counter electrode and a Whatman glass microfiber membrane as the separator. The electrolyte used was a 1 M $LiPF_6$ solution in ethylene carbonate (EC)/dimethyl carbonate (DMC) (1:1 v/v). The electrochemical performance was evaluated by carrying out galvanostatic charge–discharge tests at a current density of 100 mA/g and between 0.05 and 3.0 V, with a 10 minute rest at the end of each discharge cycle. The rate capabilities for both electrodes were evaluated at different current densities: 50 mA/g, 100 mA/g, 200 mA/g, 400 mA/g, and 500 mA/g. The specific charge/ discharge capacities were calculated based on the mass of the flexible nanofiber anodes. The cyclic voltammetry and impedance experiments were evaluated using an electrochemical impedance spectroscope (Autolab 128N) with a scan rate of 0.5 mV/s between 0 and 3 V and frequency of 0.1 Hz and 1 kHz, respectively.

The impedance for the fresh (uncycled) Sn/C cells and the aged cells after cycling was carried out using an electrochemical impedance spectroscope (Autolab 128 N) at frequencies of 0.1 Hz and 1 kHz. The measured impedances of the batteries were fit using the equivalent circuit model shown in Fig. 14a (insert) to determine parameters such as the SEI film resistance, the Ohmic resistance, charge transfer resistance, double layer capacitance, and the Warburg impedance of the battery. In the model, R_0 presents the Ohmic resistance caused by the electrolyte, deposit layer, separator, current collector, and the electrode, which equals to the left intercept between impedance spectrum and the x-axis at

Table 1
The average pore size, pore volume, and BET surface area of the various composite fibers.

Microstructure.			
Sample	Pores Size (Å)	Pores Volume (cm^3/g)	Surface Area (cm^2/g)
SnO_2/NiO/CNFs	31.84	0.136	171.24
Sn/CNFs	21.89	0.305	575.28
CNFs	19.98	0.151	301.71
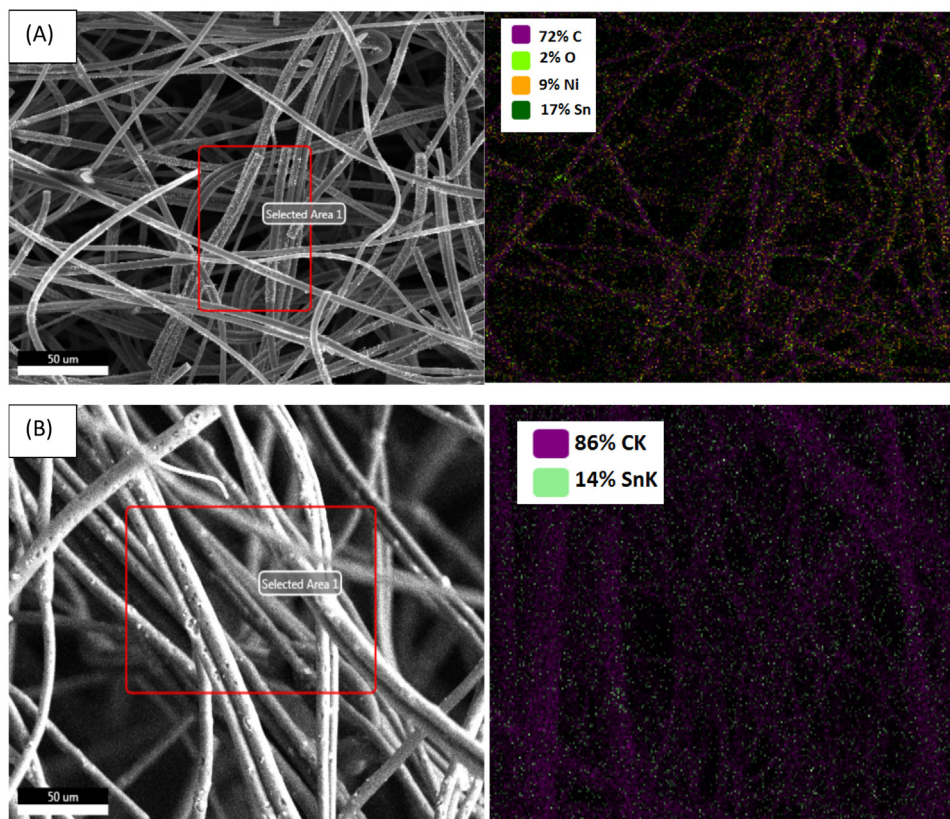
Fig. 2. EDAX area mapping of $SnO_2/NiO/C$ composite nanofibers (a) and that of the Sn/C composite nanofibers (b) the $SnO_2/NiO/C$ composite electrode shows the distribution of the Sn, Ni, and C on the composite fiber mat.
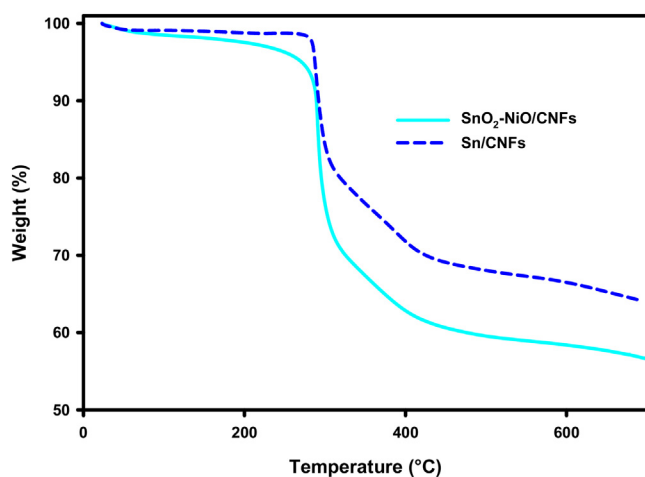
Fig. 3. TGA analysis of the $SnO_2/NiO/C$ and Sn/C composite fibers showing the actual carbon content in the electrodes.

high frequency ($\sim$1 kHz), R_{sei} and C1 indicate SEI resistance and constant phase element (CPE) at the anode, which dominates the shape of the first semi-circle in high frequency domain from 1 kHz to several Hz. While Rc and C2 indicate charge transfer resistance and double layer capacitance, respectively. They affect the shape of the second semi-circle, which is less obvious in the lower frequency range (several Hz to several mHz). On the other hand, Wa is the Warburg admittance, which represents ion diffusion in the solid electrode. The Warburg admittance dominates the impedance spectrum in the low frequency region ($<$several mHz). To extract these parameters, the EIS-ECM was fitted to

the impedance spectrum measured by EIS using a simplex algorithm.

3. Results and discussion

3.1. Surface morphology and elemental analysis

The SEM micrographs of the Sn/CNFs and $SnO_2/NiO/CNFs$ composite nanofibers are shown in Fig. 1a and b, respectively. After carbonization at 800 °C in an inert environment for 2 h the Sn/PAN and $SnO_2/NiO/PAN$ precursor nanofibers were transformed to Sn/C and $SnO_2/NiO/C$ composite nanofibers. The average diameters of the nanofibers from the SEM images ranged from 100–300 nm. The Sn nanoparticles can be clearly seen on the surface of both Sn/C and $SnO_2/NiO/C$ composite nanofibers. The SnO_2 and NiO particles in the $SnO_2/NiO/C$ composite nanofibers were "hairy-like" on the fiber strands (Fig. 1b). Another feature of these fibers was the presence of many pores in the fiber strands that were evenly distributed. In particular, the pores on the Sn(nanoparticle)/C fibers had a pore volume of 0.305 cm^3/g which is larger than that for the $SnO_2/NiO/C$ composite nanofibers (i.e. 0.136 cm^3/g), as illustrated in Table 1, although the pore size for the $SnO_2/NiO/C$ was much larger. These pores contributed to the buffering effect that provided the accommodation for the volume change during the alloying and de-alloying process of Sn and SnO_2/NiO with lithium. The pores on the composite nanofiber anode were created during the calcination process via the passage and interaction of the inert gas molecules with the nanofibers.

The elemental mapping analysis (i.e. EDAX) of the composite Sn/C and $SnO_2/NiO/C$ nanofibers (Fig. 2) clearly shows that these composite nanofibers consist predominantly of Sn and carbon for the Sn/C composite anode and Sn, Ni, and carbon for the $SnO_2/NiO/$
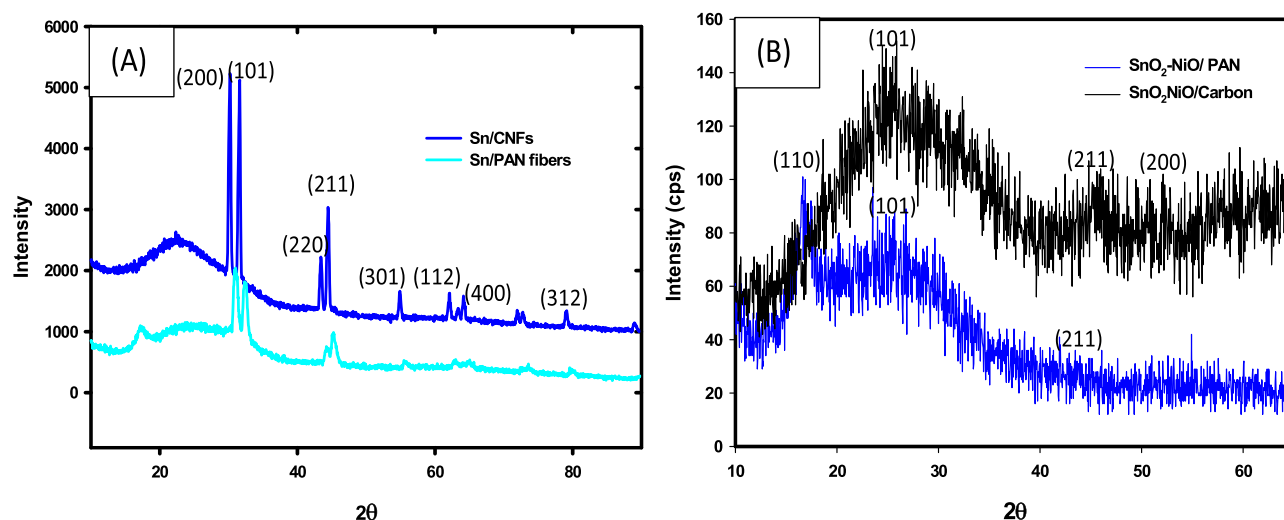
Fig. 4. XRD pattern of Sn/PAN precursor nanofibers and that of Sn/C composite nanofibers prepared from 15 wt.% Sn/PAN precursors at 800 °C(a) and that for the SnO$_2$/NiO/ PAN precursor and SnO$_2$/NiO/carbon fibers(b).

C anode. The EDAX area mapping for the composite nanofibers showed the heterogeneous distribution of the composite electrode constituents in the carbon matrix. The area mapping clearly shows that the composite electrode predominantly consists of carbon. The actual content of carbon and the cations in the composite nanofibers were determined by TGA analysis (Fig. 3). It can be seen in Fig. 3 that up to 92 °C, a minor weight reduction of ∼3% which corresponds to the removal of physically absorbed water from the fibers, was observed for both composite electrodes. At temperatures between 290 °C and 410 °C, there is a multistage decomposition that could be attributed to the polymer (polyacrylonitrile), which recorded a weight loss of ∼38% for the Sn/C composite electrode. For the SnO$_2$/NiO composite nanofiber, the multistage decomposition was observed at temperatures 320 °C and 410 °C. The oxidation of carbon for both Sn/C and SnO$_2$/NiO/C was observed above 450 °C, and beyond 530 °C while the weight loss remained steady. The TGA results indicate that the composite nanofibers contained ∼64 wt% and ∼58 wt% of carbon for the Sn/C and SnO$_2$/NiO/C fibers, respectively.

3.2. Analysis of the crystal structure of the composite electrodes

X-ray diffraction (XRD) analysis of the as-synthesized Sn/PAN and SnO$_2$/NiO nanofiber precursors along with their respective composite nanofiber electrodes was carried out to evaluate the crystal structure of the composite nanofiber electrodes. In Fig. 4a, the XRD pattern of Sn/C composite electrode showed the tetragonal rutile structure (JCPDS 41-1445) of the space group $P4_2/mnm$. The peak at the 18° followed by a broad peak is attributed to the un-stabilized PAN polymer in the Sn/PAN nanofiber precursor (Fig. 4a). This small peak disappears after carbonization but the broad amorphous peak still remains after the carbonization process. The broad peak in the calcined Sn/C could indicate the presence of hard carbon or non-graphitized carbon in the carbon fibers. During the carbonization process of Sn/PAN nanofibers at 800 °C in an inert atmosphere, the PAN polymer is converted into carbon fibers, while the Sn could have been oxidized to SnO$_2$ during the stabilization process at 280 °C and back to the metallic phase at 800 °C during the carbonization process in the inert environment. However, it is expected that some amount of the oxide will still exist in the final product of Sn/C composite electrode. The peak pattern obtained in the X-ray shows a small amount of SnO$_2$ [40] and metallic Sn. The peaks of the metallic Sn

were observed as doublet at 43° in the as-forcespun Sn/PAN fibers. The carbonization process completely separates the shoulder of the peak of the metallic Sn in the forcespun Sn/PAN nanofibers into two distinct peaks indexed as (220) and (211). Additionally, there was a shift of the (200) and the (101) peaks to a lower 2θ relative to the baseline, which is indicative of an improvement in the interplanar layer spacing in the Sn/C crystal structure. Another difference in the XRD patterns is the relative intensity ratio of XRD peaks of the as-spun Sn/PAN nanofibers and that of the Sn/C composite electrode which is attributed to the difference in crystallinity and crystal size. For the SnO$_2$/NiO/C composite electrode and SnO$_2$/NiO/PAN precursor fiber, the XRD pattern in Fig. 4b shows several broad peaks of low intensity for both the precursor fiber and the carbonized fibers. These broad peaks are attributed to the low crystallinity level on these fibers. The broad peaks at 26° and 43° indexed to (101) and (211) are identified as the planes of tetragonal rutile SnO$_2$ (JCPDS41-1445), while the cubic NiO are indexed at (200) plane (JCPDS71-1179). However, the NiO peak was not obvious on the SnO$_2$/NiO/PAN fiber XRD pattern. The carbon peak pattern was not observed, which could be attributed to the amorphous structure of carbon in these nanofibers. The lack of distinct peaks for the SnO$_2$ and that of the NiO in the carbonized fibers are indication of the amorphous nature of these compounds in the carbon fiber matrix.

3.3. Surface analysis (XPS)

To evaluate the composition of the surface compounds on the Sn/C nanofibers and that of the carbonized SnO$_2$/NiO/C composite nanofibers, a high resolution XPS analysis was carried out. The XPS results shows the survey spectra in Fig. 5a as well as those for the C1s, O1s, and the Sn 3d peaks for the composite electrode of Sn/C. The C1s peak for both the Sn/C and SnO$_2$/NiO nanofibers show a broad peak, which was de-convoluted into two peaks at 284.6 eV and 285.6 eV. Typically, the binding energy with the peak at 284.6 eV is often associated with the C-C bonds and attributed with the amorphous carbon phase or from adventitious carbon, while the peak at 285.6 eV was characteristic of the combination of C-O or the carboxyl (i.e. O—C=O) groups that could have served as the nucleation point for the SnO$_2$ [41,42]. The spectra for the Sn 3d revealed the spin–orbit components (3d$_{3/2}$ and 3d$_{5/2}$) of the Sn 3d peaks at binding energies ∼495.3 and ∼486.7 eV for both as shown in Fig. 5a for the Sn/C and SnO$_2$/NiO/C composite nanofibers in
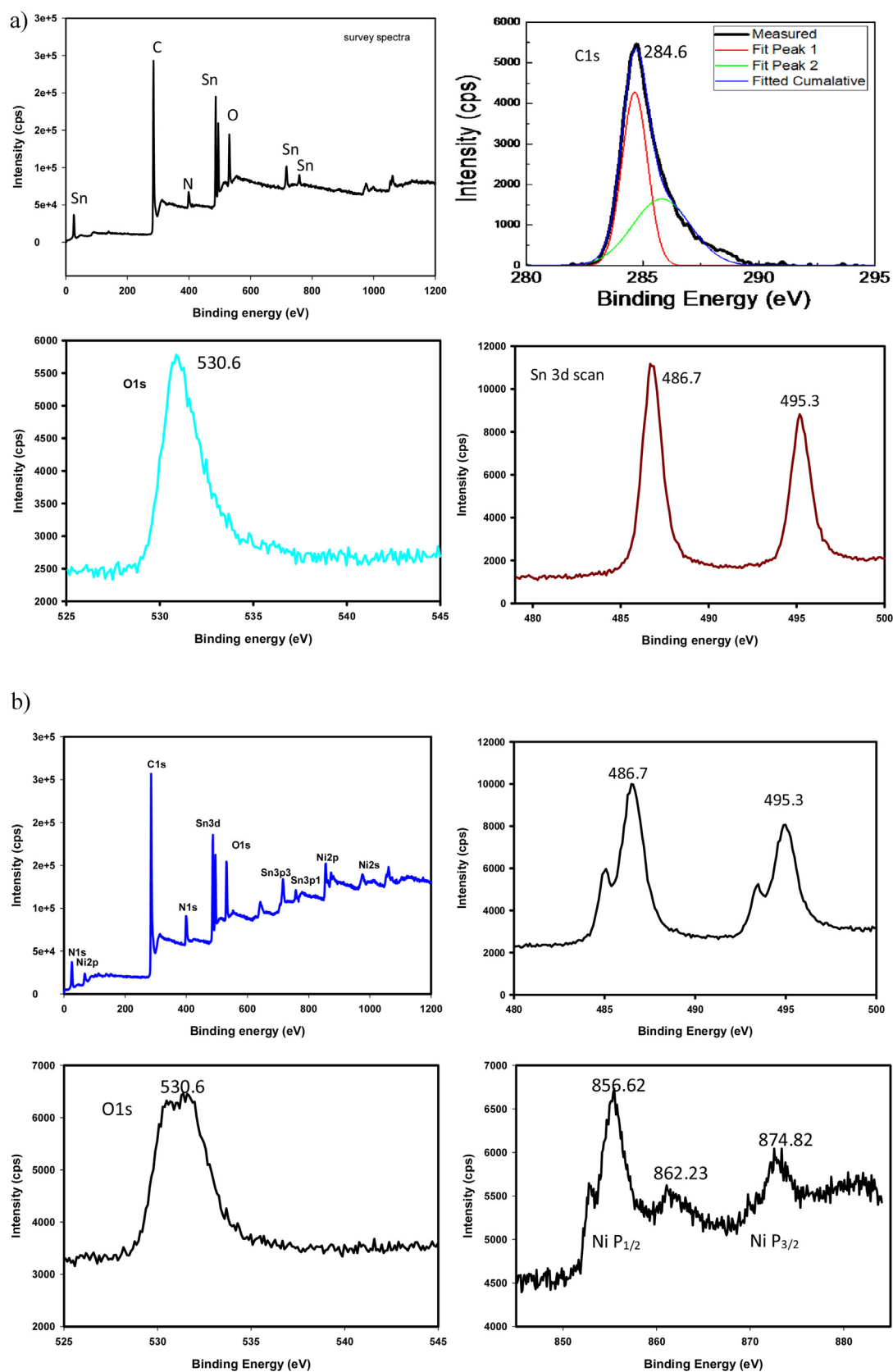
Fig. 5. a. XPS spectra of C 1s, O1s, and Sn3d for Sn/C composite nanofibers. b. XPS spectra showing a survey spectra, the spectra of C1s, O1s, Sn3d, and Ni1s for the SnO$_2$/NiO composite nanofibers. With the Sn3d and Ni1s showing distinct peaks with shoulders compared to that observed in the Forcespun SnO$_2$/NiO nanofibers.

a)

b)
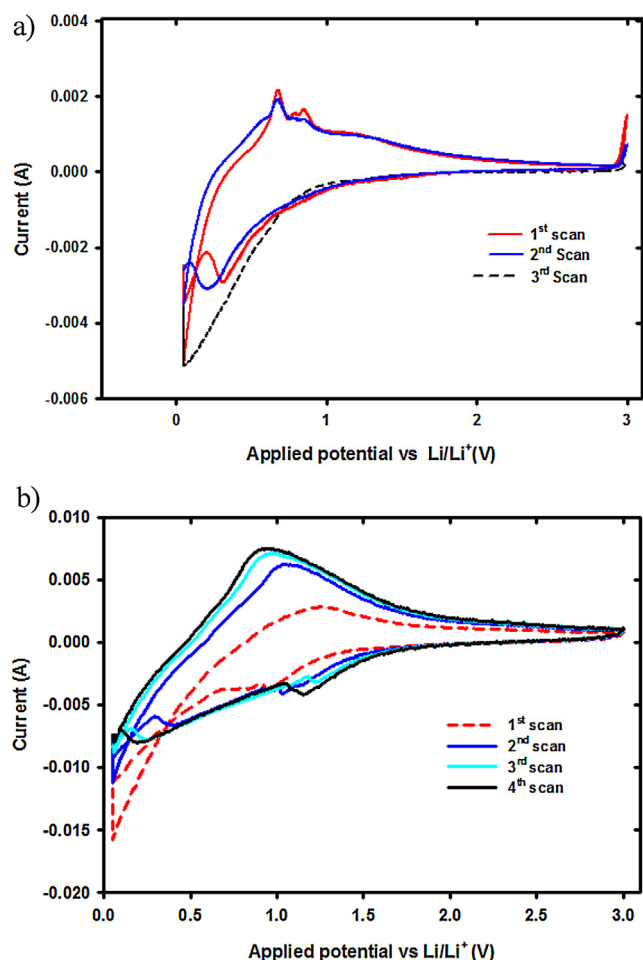
Fig. 6. a. Cyclic voltammogram (CV) of Sn/C composite NFs in half-cell configuration between 0.005–3 V vs. Li at scan rate of 0.2 mVs^{-1}. b. Cyclic voltammogram (CV) of carbonized SnO$_2$/NiO/C composite nanofibers in half-cell configuration between 0.005–3 V vs. Li at scan rate of 0.2 mVs^{-1}.

Fig. 5b. In the SnO$_2$/NiO Sn 3d spectra, there were two shoulder peaks on the 3d$_{3/2}$ and 3d$_{5/2}$ that were absent in the Sn/C nanofibers, these shoulder peaks could not be immediately explained. However, the splitting of the 3d doublet of Sn at 8.6 eV, indicates a probable valence state of Sn to be +4 [43] (i.e. Sn^{4+} in the SnO$_2$). For the Sn/C nanofibers, this phenomenon further enforces the formation of small amounts of SnO$_2$ nanoparticles as part of the Sn/C composite electrode structure. The XPS spectra for the O1 s scan in both composite nanofibers showed one peak at binding energy 530.6 eV and assigned to the O in the SnO$_2$. These results thus point to a heterogeneous structure from the composite nanofibers comprising SnO$_2$ nanoparticles embedded in the carbon nanofibers for the Sn/C and SnO$_2$/NiO composite anodes. In the SnO$_2$/NiO nanofibers, the main Ni2p$_{3/2}$ peak at 856.62 eV, its satellite peaks at 862.96 eV, 874.86 eV, and 881.28 eV shown in Fig. 5b are attributed to NiO [44] and there were not attributable to Ni metal in the spectra, suggesting that the residual Ni in the fibers was insignificant.
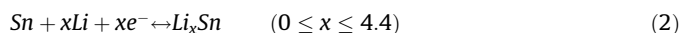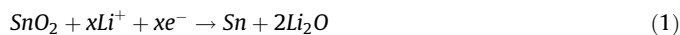
3.4. Electrochemical performance

3.4.1. Cyclic voltammogram for the Sn/C composite NF anode

Cyclic voltammetry (CV) test was carried out on the Sn/C and SnO$_2$/NiO composite nanofiber electrodes to evaluate the Lithium storage properties. A half-cell configuration of these electrodes was constructed and the CV test was performed between 0.0-3.0 V

vs. Li/Li$^+$ at slow scan rate of 0.2 mV s^{-1}. The CV curves for the SnO$_2$/NiO and Sn/C electrodes are shown in Fig. 6a and b, respectively. During the first cathodic scan, the test Sn/C cells exhibited a broad and sharp peak potential at ~0.38 V vs. Li/Li$^+$, which is attributable to the structural destruction of Sn/SnO$_2$ and associated initial electrolyte decomposition [45].

The decomposition reaction of the electrolyte solution with Li leads to the formation of a solid electrolyte interface (SEI) on the composite nanofiber anodes/electrolyte interface. In this case, the SEI layer will mainly consist of lithium carbonate and lithium alkyl species. The structural destruction of SnO$_2$ species in the SnO$_2$/NiO/C composite electrode leads to the formation of amorphous Li$_2$O according to the partially reversible equilibrium equation;

$$SnO_2 + xLi^+ + xe^- \rightarrow Sn + 2Li_2O \tag{1}$$

$$Sn + xLi + xe^- \leftrightarrow Li_xSn \qquad (0 \leq x \leq 4.4) \tag{2}$$

$$C + xLi^+ + xe^- \rightarrow Li_xC \tag{3}$$

The formation of Li$_2$O on the electrode was confirmed from the CV curve of the SnO$_2$/NiO/C nanofiber electrode and exhibited at potential 1.2 V vs Li/Li$^+$ [46], which continues to increase after each scan. However, for the Sn/C composite electrode, the Li$_2$O peak was absent during the cathodic sweep, therefore Reaction (1) could not have occurred in the case of Sn/C composite electrode. Therefore the amount of SnO$_2$ in the electrode was considered insignificant in the Sn/C nanofibers.

The presence of a peak potential at ~0.23 V vs. Li/Li$^+$ for both electrodes is associated with the reversible alloying formation process between the Sn and lithium according to the following reaction;

$$Sn + xLi^+ + xe^- \leftrightarrow Li_xSn, 0 \leq x \leq 4.4 .$$
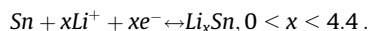
Again during the anodic sweep, the peak potential of ~0.82 V vs. Li/Li$^+$ corresponds to the de-alloying reaction according to the reduction reaction above. During this de-alloying process, it is possible that electrochemically formed Sn nanoparticles could aggregate to form large clusters in order to reduce surface free energy. It is the formation of such large clusters that normally lead to the cracking of the electrodes and the eventual increase in the cell's internal resistance.

The storage/cycling performance of the Sn/C composite anode was investigated at room temperature. The charge/discharge curves for the Sn/C and that of the SnO$_2$/NiO/C composite nanofibers electrode, for the first 100 cycles were obtained at a voltage between 0.05 V and 3.0 V and at a current density of 100 mA/g. The presence of SnO$_2$ in SnO$_2$/NiO/C and small amounts for the composite Sn/C electrode initiates the general electrochemical reactions in Equations 1-3 and presented schematically in Fig. 7. This reaction gave a first initial specific discharge capacity of 589 mAhg^{-1} for the baseline CNFs electrode (Fig. 8a), 2586 mAhg^{-1} for the Sn/C composite anode (Fig. 8c), and 1885 mAhg^{-1} for the SnO$_2$/NiO/C composite electrode (Fig. 8b). A current density of 100 mA g^{-1} was used for the first discharge step to allow greater amount of Li$^+$ into the composite electrode structure. These capacities are remarkably higher than those reported in various literatures [47,48] on the Sn/C or SnO$_2$/C composite nanofiber electrodes. There was a steady drop in the discharge capacity for all electrode; SnO$_2$/NiO/C, Sn/C as well the baseline CNFs composite anodes from the 1st to the 10th cycles, which are consistent with results reported in literature [8,49,50].

The drastic drop in capacity is often associated with inevitable irreversible loss of lithium ions for the formation of the solid
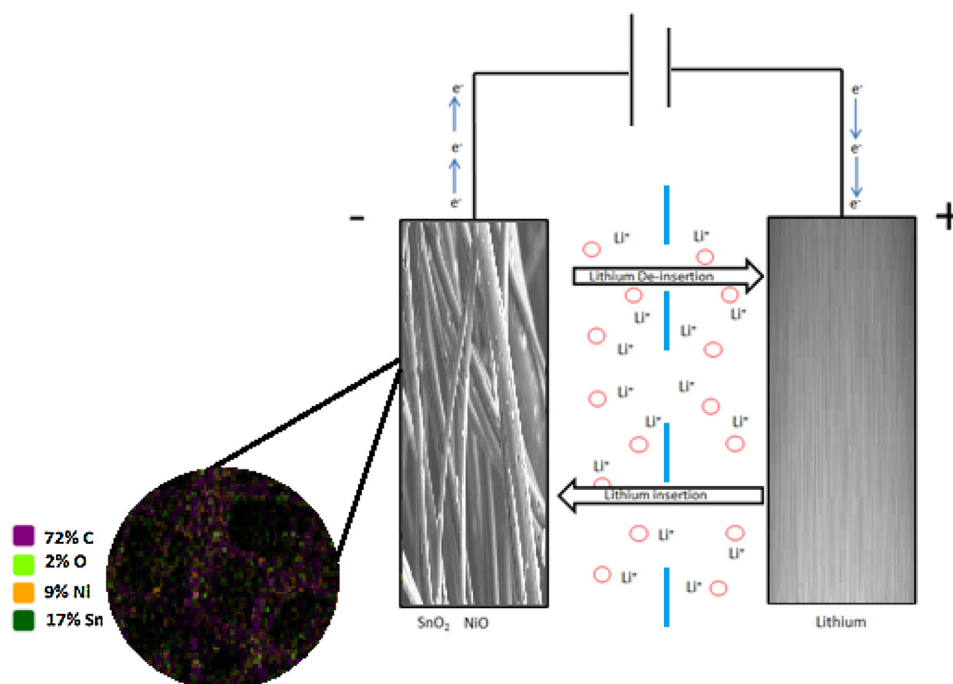
Fig. 7. Schematic of Lithium insertion/Lithium de-insertion process that occurs within the half-cell upon cycling.

electrolyte interface layer. Unlike in many other battery chemistries such as the over lithiated cathodes; $Li_{x+1}FePO_4$ and $Li_xMn_{1-x}NiCoO_4$ where extra lithium is provided for in the electrode to compensate for amount of lithium used for the SEI layer formation, the composite nanofiber electrode do not have that extra Li^+ for this purpose. Interestingly, for the $SnO_2/NiO/C$ electrode (Fig. 8b), the capacity fade existed from the 1st through to the 10th cycle and the specific capacity steadily increased. A similar trend was also observed for the Sn/C composite electrode (Fig. 8b). The steady rise of the specific discharge capacity continued the 50th and 100th cycle, with the discharge capacity almost equal to that of the 2nd discharge capacity (i.e. ∼85% capacity recovery) for the $SnO_2/NiO/$composite electrode. On the other hand, the Sn/C composite electrode had a steady recovery of the faded capacity after 10th cycle up to the 50th cycle, which had a discharge capacity significantly greater than that at the 10th cycle. However, there was a significant second capacity fade that was observed after 50th cycle, i.e. from 714 mAg^{-1} to 677 mAg^{-1} at the 100th cycle. The second capacity fade was not observed in the $SnO_2/NiO/C$ composite electrode. The Sn/C composite anode on the other hand, showed less irreversible capacity loss at the second cycle than that for $SnO_2/NiO/C$ composite nanofibers electrode, with the $SnO_2/NiO/C$ losing almost half of the 1st discharge capacity on the 2nd cycle. This is often attributed to SnO_2 content in $SnO_2/NiO/C$ anode, the oxygen-containing functional groups on the SnO_2/NiO fibers react with Li^+ resulting in the irreversible loss of recyclable lithium ions [51,52]. The electrochemical performance for the baseline progressively decreased from the 1st to the 50th cycle, thereafter it remained steady at 124 mAg^{-1} at the end of the 100th cycle. When the contribution of carbon nanofiber in the composite electrode (i.e. 124 mAg^{-1}) is taken out, the Sn and the SnO_2/NiO would have specific capacities of 509 mAhg^{-1} and 551 mAhg^{-1} respectively for the 100 cycles, which is significantly impressive.

The cycling performance for both composite electrodes is shown in Fig. 9. The results shown in Fig. 9 indicate that the Sn/C composite nanofibers, which had a much higher initial discharge capacity compared to the $SnO_2/NiO/C$ composite electrode cell, maintained a steady capacity of 675 mAg^{-1} compared to 633 mAg^{-1} for the $SnO_2/NiO/C$ composite electrode. The slight

difference in capacity between the two electrodes was not that significant after the 100th cycle, considering that fact, the addition of NiO to the SnO_2 was aimed at improving the conductivity. This notwithstanding, the Sn/C composite nanofiber electrode appeared to have a little improved capacity retention over the $SnO_2/NiO/C$ binary composite electrode. Statistically, the subtle difference between the specific capacities of the two composite electrodes was the same. Furthermore, even after 100 deep charge/discharge cycles, both cells maintained a Coulombic efficiency >95% as shown in Fig. 9. The relatively higher capacity of these composite nanofiber electrodes is most importantly due to the quality of the nanofiber produced using the Forcespinning method, which produced fibers with unique microstructures that include pores and hairy-like microstructure, capable of buffering the volume change associated with Sn/C and $SnO_2/NiO/C$ electrode during the alloying/de-alloying process. The porous structure of these composite nanofibers also contributed to improving their cycle performance. Most reported literature using binder free electrodes from electrospinning and centrifugal spinning show [48,53] lower discharge capacities ranging from 400 to 650 mAhg^{-1} after 50 cycles.

A postmortem (tear-down) analysis was carried out on the cycled cells after undergoing 100 cycles to elucidate any changes in the materials structure and morphology. The morphology of the aged $SnO_2/NiO/C$ electrode as shown in Fig. 10, consisted of a heavily passivated layer on the surface of the fiber strands.

The formation of the passivation layer on the fiber strands could be explained as follows; in the electrolyte solvent mixture of EC and DMC, the high polarity and dielectric constant of ethylene carbonate compared to the DMC, will position it to preferably undergo a reduction reaction[54]. The reduction of EC involves a two-electron transfer to one mole EC and reaction with Li^+ to produce Li_2CO_3 and C_2H_4 gas (Eq. (1)).

$$EC + 2e^- + 2Li^+ \rightarrow (CH_2OCO_2Li)_2 \downarrow +CH_2 = CH_2(g) \uparrow \qquad (1)$$
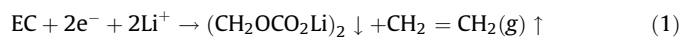
Subsequently, the species $(CH_2OCO_2Li)_2$ in Eq. (1) on the composite carbon SnO_2/NiO electrode surface, can readily react with traces of

a)

b)

c)
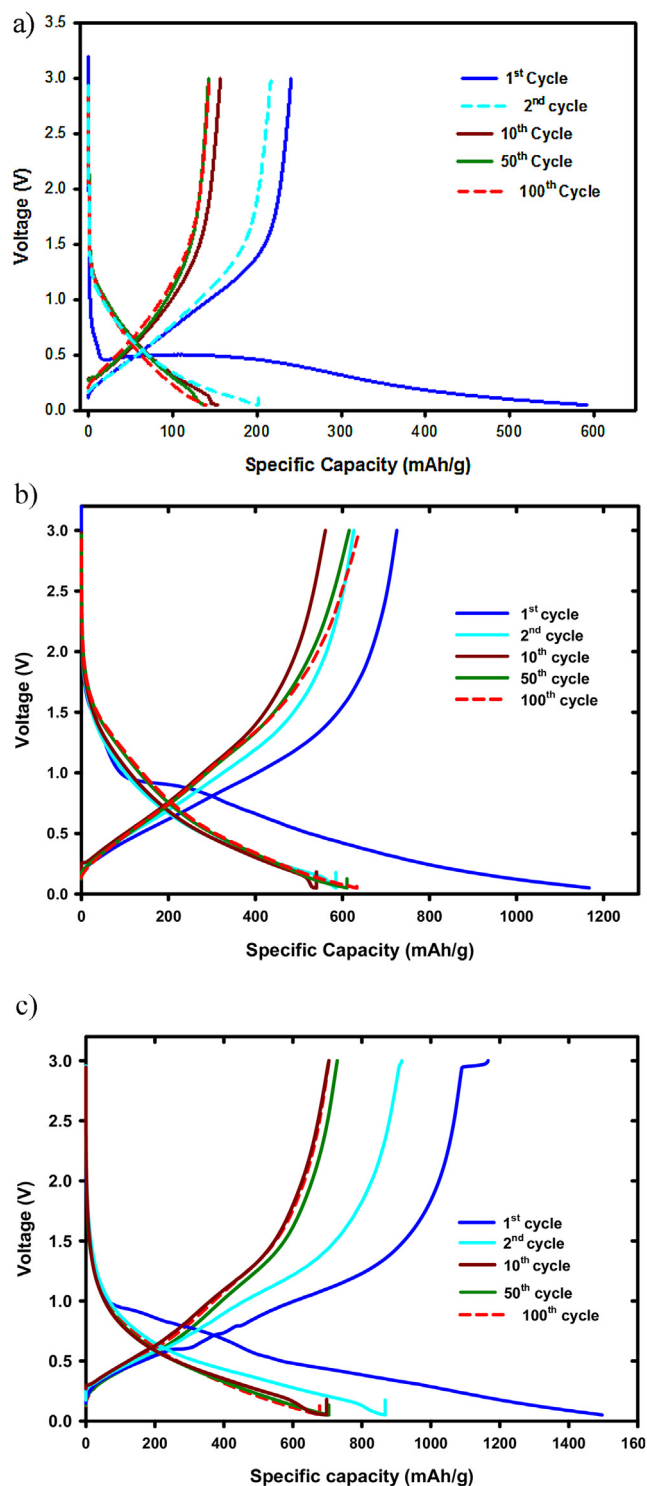
Fig. 8. a. Galvanostatic charge/discharge curves of carbon nanofiber (CNF) electrode made from PAN precursor at a current density of 100 mAg^{-1} with a voltage window of 0.05–3.0 V. b. Galvanostatic charge/discharge curves SnO$_2$/NiO/C composite electrode made from SnO$_2$/NiO/PAN precursor nanofibers at a current density of 100 mAg^{-1} with a voltage window of 0.05–3.0 V. c. Galvanostatic charge/discharge curves Sn/C composite electrode made from Sn/PAN precursor nanofibers at current density of 100 mAg^{-1} with a voltage window of 0.05–3.0 V.
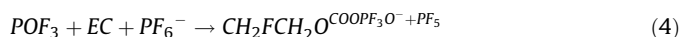
H$_2$O either in the solution or in the working environment (i.e. glovebox) to produce Li$_2$CO$_3$, (CH$_2$OH)$_2$ and CO$_2$ gas (Eq. (2)) [55].

$$(CH_2OCO_2Li)_2 + H_2O \rightarrow Li_2CO_3 \downarrow + (CH_2OH)_2 \downarrow + CO_2(g) \uparrow \qquad (2)$$
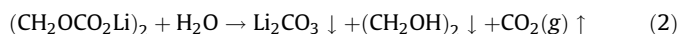
The reaction with H$_2$O could therefore compound the amount of gases produced in the cell leading to cell venting. It is therefore imperative to keep the H$_2$O content in the glovebox to minimal levels (<0.5 ppm).

The formation of these species form part of the solid electrolyte interface (SEI) on the composite electrode surface. However, after prolong cycling, the SEI layer structure may be distorted, thus exposing the composite electrode surface to more electrolyte decomposition reaction. In particular, the decomposition species of POF$_3$ and PF$_6$ – from the unstable lithium salt, LiPF$_6$ undergoes a reduction reaction with EC to produce various species (Eqs. (3) and (4));

The salt dissociates into LiF and the Lewis acid PF$_5$ (Eq. (3));

$$LiPF_6 \leftrightarrow LiF + PF_5 \qquad (3)$$

$$POF_3 + EC + PF_6^- \rightarrow CH_2FCH_2O^{COOPF_3O^- + PF_5} \qquad (4)$$

which can dissociate further to form an additional anion in solution (Eq. (5))

$$CH_2FCH_2OCOOPF_3O^- + PF_5 \rightarrow CH_2FCHOCOOPF_2O + PF_6^- \qquad (5)$$
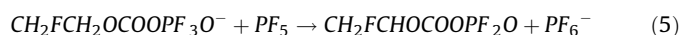
Which can initiate an autocatalytic process to perpetuate the decomposition reaction [34].

The surface species PF5 was identified as a possible compound on the aged SnO$_2$/NiO/C and Sn/C composite electrodes as evident in qualitative analysis (EDS) of the aged electrode in Fig. 10d.

The crystal structure analysis of the aged SnO$_2$/NiO/C and that of the Sn/C electrode were again analyzed after the aging process (Fig. 11). The X-ray pattern for the aged vs the fresh electrode of SnO$_2$/NiO/C (Fig. 11a) shows a general reduction in the amorphous peak at lower 2θ, a shift of the peaks to higher 2θ, broadening of the peaks, and emergence of two new phases for the aged electrode. The broadening and peak shift was indicative of lithium residing in the host electrode, although the cell was discharged to 0.01 V, it is expected that some amount of lithium will remain in the crystal structure of the electrode. The two new phases on the aged SnO$_2$/NiO/C electrode were identified to belong to the electrolyte species of LiF and possibly PF$_5$, which correlates the qualitative results from the EDS analysis in Fig. 10d. For the aged Sn/C electrode, there was neither a peak shift nor peak broadening observed relative to its fresh electrode x-ray diffraction pattern. However, four new phases, two observed at 32° and 38° and similar to those found in the aged SnO$_2$/NiO/C electrode were also attributed to the presence of the electrolyte species LiF and PF$_5$. The other two phases were observed at lower 2θ i.e. at 22° and 24°, the sharp peak at 22° was identified as that of graphite peak indexed (002), the appearance of the graphite peak along with that at 22° on the aged Sn/C electrode could not readily be explained. These electrolyte decomposition species, in particular LiF form a resistive layer on the fiber surface, which negatively affected the Li$^+$ transfer. This was manifested amply in the impedance for both SnO$_2$/NiO/C and Sn/C aged electrode in Fig. 14(a and b) where there was an increase in the impedance of their respective aged electrode relative to the baseline.

The suitability of these alternative nanofiber composite electrodes was further evaluated by performing a rate capability test at different current densities: 50, 100, 200, 400, and 500 mAg^{-1} and cycling for just 10 cycles as shown in Fig. 12. In all these rate capability tests, the SnO$_2$/NiO/C composite electrode exhibited a much higher discharge specific capacity compared to the Sn/C composite electrode cells. Another observed phenomenon was the steady stabilization of the capacity fade of the Sn/C composite electrode at 50 mAg^{-1}, 100 mAg^{-1}, 200 mAg^{-1}, and even at 500 mAg^{-1} compared to a steep loss and slower stabilization of
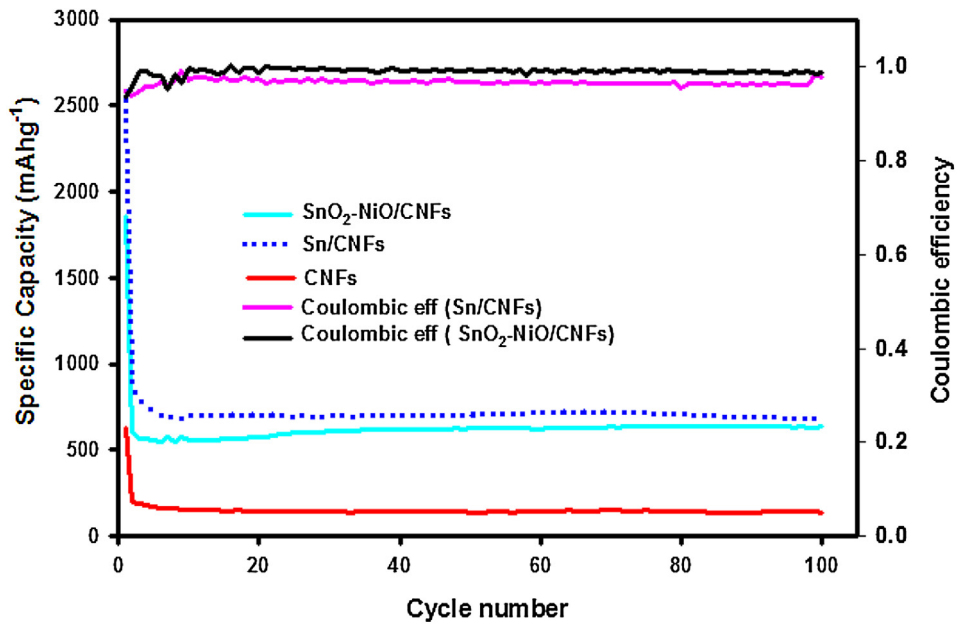
Fig. 9. A comparison of the cycle performance of the SnO₂/NiO/CNFs and Sn/CNFs composite electrodes at 100 cycles cycled between 0.05V–3.0 V potential.
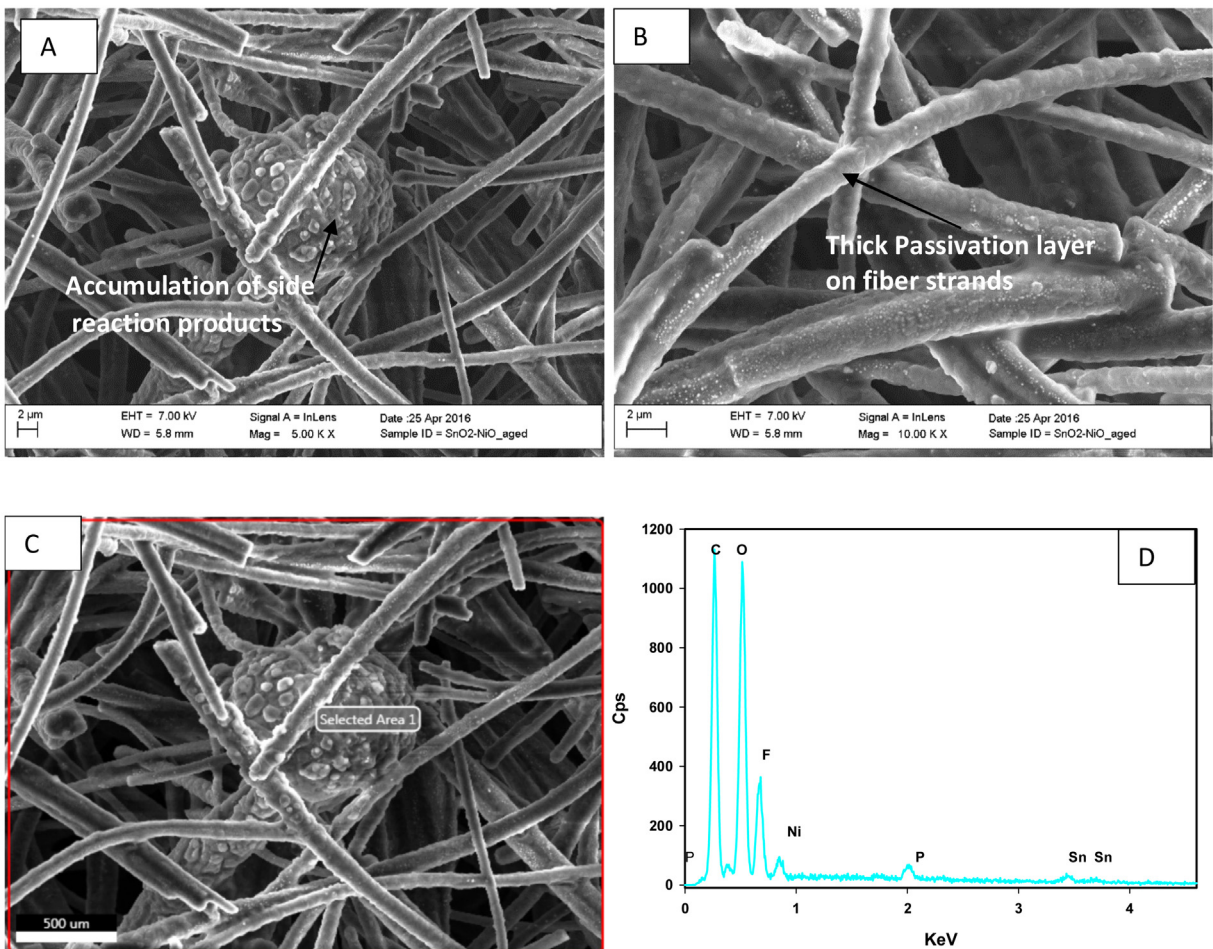

Fig. 10. SEM images of aged Sn/C (a) SnO₂/Nio/C (b) and electrode after 100 cycles. EDS micrograph with corresponding spectra of elements (d) on the surface of the aged SnO₂/NiO/C electrode.
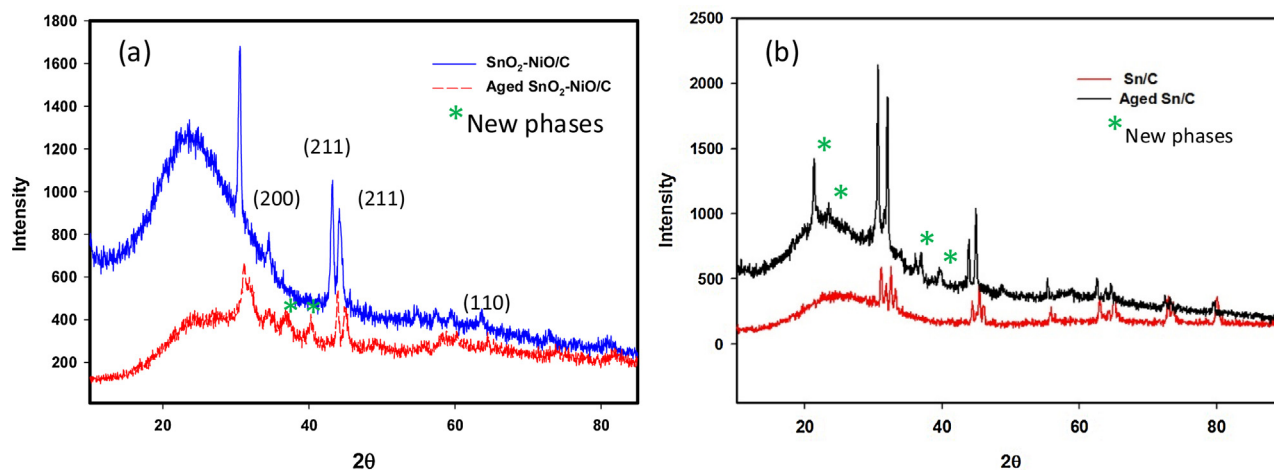
Fig. 11. XRD pattern of the aged (a) SnO$_2$/NiO/C and Sn/C (b) composite electrode after undergoing 100 cycles.
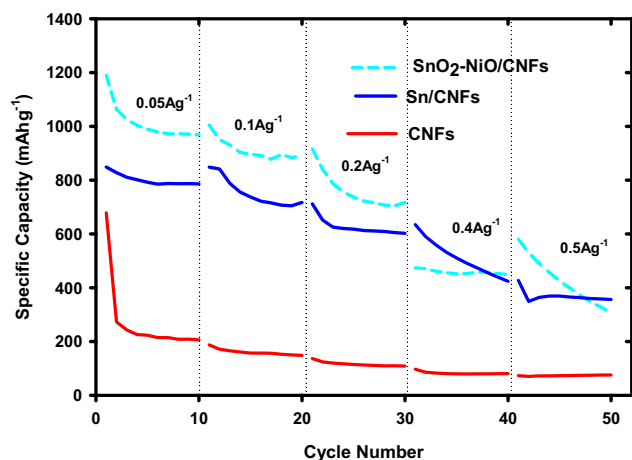
Fig. 12. Rate performance of the SnO$_2$/NiO/C and Sn/C composite electrode at various current densities from 50 mA/g to 500 mA/g over 10 cycles between 0.05–3.0 V.
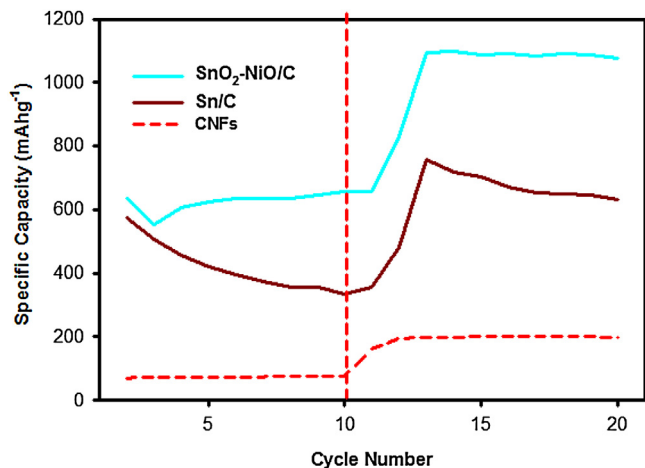

Fig. 13. Capacity recovery after cyclic current performance for the Sn/C and SnO$_2$/NiO/C composite electrodes.

the SnO$_2$/NiO/C composite electrode. At the 400 mAg^{-1} cycling, however, the SnO$_2$/NiO/C capacity was nearly stable while that of the Sn/C had a steep drop in the capacity that showed no steadiness over the 10 cycles, much like capacity fade behavior of the SnO$_2$/NiO/C electrode observed at the 500 mAg^{-1} region. The good performance in terms of capacity stability of the Sn/C composite electrode is attributed to the large and evenly distributed pores on the fibers, which offered a much more buffering to accommodate the volume change during the alloying/de-alloying process. On the other hand, the recorded higher capacity of the binary SnO$_2$/NiO/C composite electrode was attributed to the presence of NiO. The NiO provided the needed structural stability of the electrode that prevented it from pulverization, while at the same time enhanced the electrical conductivity of the electrode [2,20,56].

The capacity recovery after applying a cyclic current was evaluated. In this test, the cells were cycled at 500 mAg^{-1} for 10 cycles and the cell rested an hour to achieve electrochemical stability and then charge/discharge tests were performed for 10 cycles at a low current density of 50 mAg^{-1}. The electrochemical performance of the Sn/C and SnO$_2$/NiO/C composite fiber anodes subjected to this current cyclic test is shown in Fig. 13. In this capacity recovery test, the Sn/C electrode had a gradual capacity fade during the 500 mAg^{-1} cycle compared to an initial dip follow by a gradual steady stabilization of the capacity observed from the SnO$_2$/NiO/C composite electrode. When the cycling current was ramped down to 50 mAg^{-1}, as expected, the capacities of both electrodes increased dramatically. The SnO$_2$/NiO/C electrode capacity became steady and recorded a capacity comparable to that recorded in Fig. 12 for 50 mAg^{-1} rate performance. However, a rather continual capacity fade was observed for the Sn/C electrode for the 50 mAg^{-1} region. From these studies, it is observed that the SnO$_2$/NiO/C electrode has a better cycling and rate performance than that for the Sn/C electrode, although the Sn/C electrode has a slight edge over it in terms of long cycle performance stability.

3.4.2. Impedance analysis

Impedance test was carried out on the freshly assembled cells of Sn/C (Fig. 14a) and SnO$_2$/NiO/C (Fig. 14b) composite electrode and subsequently after the cells were cycled 100 times. The various components of the impedance were extracted using the equivalent circuit model (Fig. 14a insert) to the simulated impedance. The impedance test was carried out to elucidate the associated electrochemical performance. The depressed semicircles in the region of the high to middle frequency range, which represents the initial interfacial resistance and charge-transfer resistance, clearly showed a large variation between the fresh and the cycled cells for
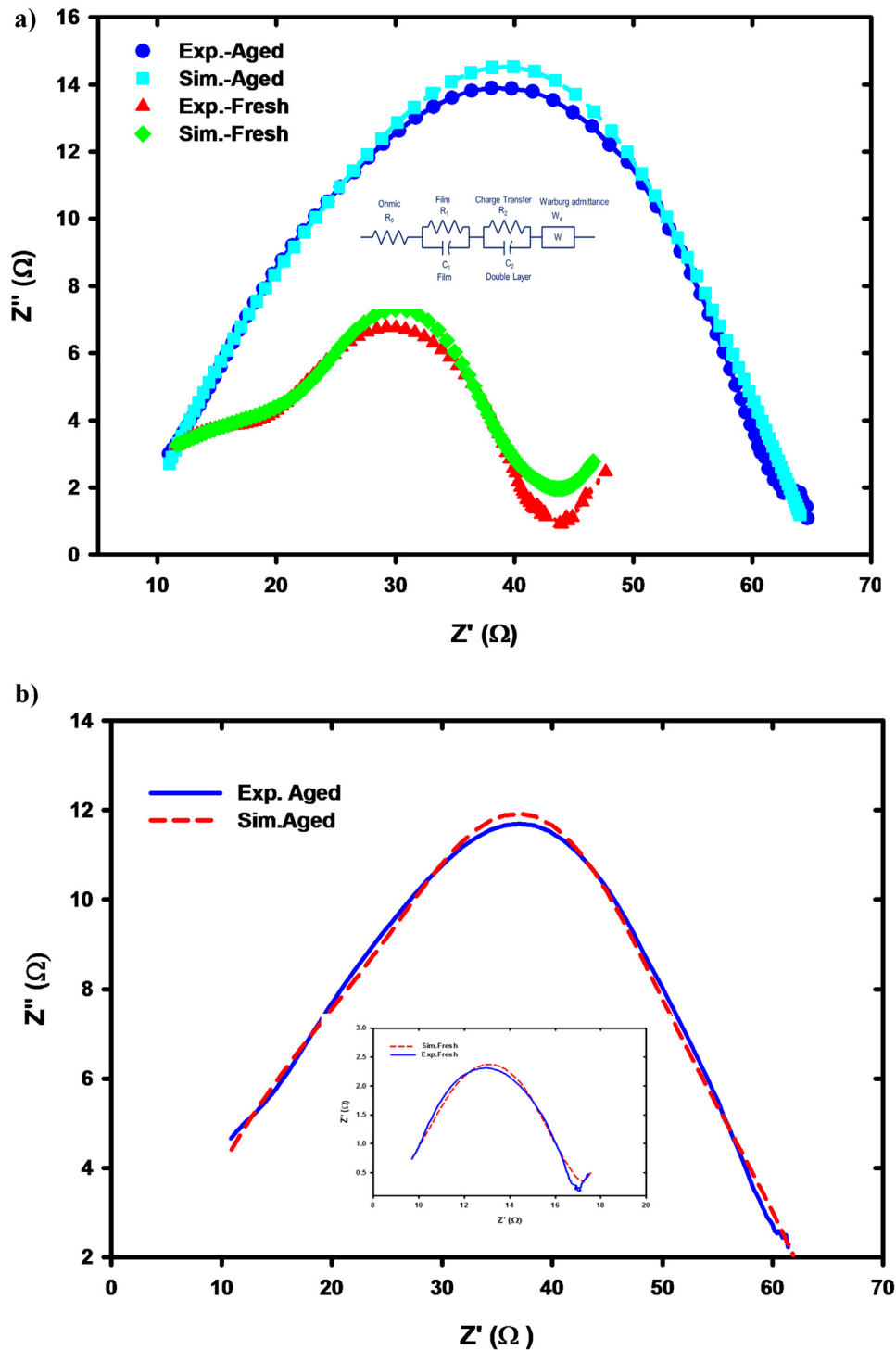
Fig. 14. a. Nyquist plots for the experimental and simulated impedance plots of the fresh and aged Sn/C electrode batteries after 100 cycles. b. Nyquist plots for the experimental and simulated impedance plots of the fresh (insert) and aged SnO$_2$/NiO/C electrode batteries after 100 cycles.

both electrodes. While the baseline (fresh) cell of the SnO$_2$/NiO/C (Fig. 14b insert) had a relative low impedance compared to that for the fresh cell Sn/C (Fig. 14a), both cell had similar impedance after aging for 100 cycles. The extracted resistances from the simulated impedance from the equivalent circuit (Table 2) showed a drastic increase in the cell ohmic resistance after cycling. There was also a

corresponding increase in the SEI layer resistance as well as the charge transfer resistance in the cell after the 100 cycles.

The increase in charge transfer and the SEI resistance at the electrode/electrolyte interface affected the lithium ion kinetics at the interface. This correlated the steady loss of capacity of the cell during the initial cycles. The electrochemical performance of the Sn/C and SnO$_2$/NiO/C composite electrode does not differ

Table 2
Extracted resistances of the aged and fresh cell of Sn/C from the equivalent circuit model (Fig. 14a insert).

		Ohmic (R_1)(Ω)	SEI (R_0)(Ω)	Charge Transfer (R_2)(Ω)
Sn/C	Fresh Cell	0.53	7.72	38.42
	Aged Cell	7.91	10.3	47.11
SnO_2/NiO/C	Fresh Cell	2.16	2.51	6.08
	Aged Cell	8.68	8.35	54.9

significantly. For the Sn/C electrode the uniform dispersion of Sn particles in the carbon nanofibers provided a large number of active sites for Li ion storage and shorter lithium ion transfer distance, while the pores in the fibers provided a pathway for ion and electron transport without the need for a current collector. All these attributes contributed immensely to the improved cycling and performance of the Sn/C nanofiber composite electrode produced by Forcespinning.

4. Conclusion

The unique morphology and structure of the composite SnO_2/NiO/C and Sn/C electrode provided a large surface area for an easy ion transport. The pores, in combination with the NiO for the SnO_2/NiO/C, provided the needed structural stability of the electrode that prevented pulverization, and enhanced the electrical conductivity of the electrode. These two factors played a key role in the improved cycle and rate performance of the binary electrode. The Sn/C nanofiber electrode, on the other hand, showed a better cycle performance and capacity retention relative to the SnO_2/NiO/C electrode. The improved cycling and rate performance of these binary nanofiber electrodes were relatively better compared to those prepared by electrospinning and centrifugal spinning system.

Acknowledgements

References

[1] X.B. Cheng, et al., Nitrogen-doped herringbone carbon nanofibers with large lattice spacings and abundant edges: Catalytic growth and their applications in lithium ion batteries and oxygen reduction reactions, Catalysis Today 249 (2015) 244–251.
[2] D. Lei, et al., Facile approach to prepare porous GeO2/SnO2 nanofibers via a single spinneret electrospinning technique as anodes for Lithium-ion batteries, Ceramics International 41 (8) (2015) 10308–10313.
[3] Y. An, et al., Mitigating mechanical failure of crystalline silicon electrodes for lithium batteries by morphological design, Physical Chemistry Chemical Physics 17 (27) (2015) 17718–17728.
[4] P.-C. Chen, et al., Hybrid silicon-carbon nanostructured composites as superior anodes for lithium ion batteries, Nano Research 4 (3) (2011) 290–296.
[5] J.S. Cho, Y.J. Hong, Y.C. Kang, Design and Synthesis of Bubble-Nanorod-Structured Fe2O3-Carbon Nanofibers as Advanced Anode Material for Li-Ion Batteries, Acs Nano 9 (4) (2015) 4026–4035.
[6] J.L. Gomez-Camer, H. Thuv, P. Novak, Electrochemical study of Si/C composites with particulate and fibrous morphology as negative electrodes for lithium-ion batteries, Journal of Power Sources 294 (2015) 128–135.
[7] G. He, et al., Bimodal Mesoporous Carbon Nanofibers with High Porosity: Freestanding and Embedded in Membranes for Lithium-Sulfur Batteries, Chemistry of Materials 26 (13) (2014) 3879–3886.
[8] H. Jiang, et al., Centrifugally-spun tin-containing carbon nanofibers as anode material for lithium-ion batteries, Journal of Materials Science 50 (3) (2015) 1094–1102.
[9] J. Wang, et al., Facile Fabrication of Binder-free Metallic Tin Nanoparticle/Carbon Nanofiber Hybrid Electrodes for Lithium-ion Batteries, Electrochimica Acta 153 (2015) 468–475.
[10] W. Li, et al., Tandem plasma reactions for Sn/C composites with tunable structure and high reversible lithium storage capacity, Nano Energy 2 (6) (2013) 1314–1321.
[11] M. Wang, et al., Hierarchical SnO2/Carbon Nanofibrous Composite Derived from Cellulose Substance as Anode Material for Lithium-Ion Batteries, Chemistry – A European Journal 21 (45) (2015) 16195–16202.
[12] I. Meschini, et al., High-performance Sn@carbon nanocomposite anode for lithium batteries, Journal of Power Sources 226 (0) (2013) 241–248.
[13] Q. Tian, et al., Facile synthesis of ultrasmall tin oxide nanoparticles embedded in carbon as high-performance anode for lithium-ion batteries, Journal of Power Sources 269 (0) (2014) 479–485.
[14] J. Chen, et al., Sn-contained N-rich carbon nanowires for high-capacity and long-life lithium storage, Electrochimica Acta 127 (0) (2014) 390–396.
[15] S. Li, J. Huang, A nanofibrous silver-nanoparticle/titania/carbon composite as an anode material for lithium ion batteries, Journal of Materials Chemistry A 3 (8) (2015) 4354–4360.
[16] Z. Shen, et al., Tin nanoparticle-loaded porous carbon nanofiber composite anodes for high current lithium-ion batteries, Journal of Power Sources 278 (2015) 660–667.
[17] J. Zhu, et al., Electrospinning preparation of ultra-long aligned nanofibers thin films for high performance fully flexible lithium-ion batteries, Nano Energy 12 (2015) 339–346.
[18] J. Zhu, et al., SnO2 Nanorods on ZnO Nanofibers: A New Class of Hierarchical Nanostructures Enabled by Electrospinning as Anode Material for High-Performance Lithium-Ion Batteries, Electrochimica Acta 150 (2014) 308–313.
[19] G. Zhang, et al., Tin quantum dots embedded in nitrogen-doped carbon nanofibers as excellent anode for lithium-ion batteries, Nano Energy 9 (2014) 61–70.
[20] B.O. Jang, S.H. Park, W.J. Lee, Electrospun Co-Sn alloy/carbon nanofibers composite anode for lithium ion batteries, Journal of Alloys and Compounds 574 (2013) 325–330.
[21] W. Xie, et al., N-Doped Amorphous Carbon Coated Fe3O4/SnO2 Coaxial Nanofibers as a Binder-Free Self-Supported Electrode for Lithium Ion Batteries, Acs Applied Materials & Interfaces 6 (22) (2014) 20334–20339.
[22] K. Sarkar, et al., Electrospinning to Forcespinning™, Materials Today 13 (11) (2010) 12–14.
[23] D. Li, Y.N. Xia, Electrospinning of nanofibers: Reinventing the wheel? Advanced Materials 16 (14) (2004) 1151–1170.
[24] S.K. Smoukov, et al., Scalable Liquid Shear-Driven Fabrication of Polymer Nanofibers, Advanced Materials 27 (16) (2015) 2642–2647.
[25] H.Z. Xu, et al., A Comparative Study of Jet Formation in Nozzle- and Nozzle-Less Centrifugal Spinning Systems, Journal of Polymer Science Part B-Polymer Physics 52 (23) (2014) 1547–1559.
[26] H.M. Golecki, et al., Effect of Solvent Evaporation on Fiber Morphology in Rotary Jet Spinning, Langmuir 30 (44) (2014) 13369–13374.
[27] P.R. Chiarot, P. Sullivan, R. Ben Mrad, An Overview of Electrospray Applications in MEMS and Microfluidic Systems, Journal of Microelectromechanical Systems 20 (6) (2011) 1241–1249.
[28] Alexander Tokarev, D.A. Ian, M. Griffiths, Oleksandr Trotsenko, Alexey Gruzd, H.A.S. Xin Lin, Sergiy Minko, Touch- and Brush-Spinning of Nanofibers, Avanced Materials 27 (41) (2015) 6526–6532.
[29] A. Tokarev, et al., Magnetospinning of Nano- and Microfibers, Advanced Materials 27 (23) (2015) 3560–3565.
[30] V.A. Agubra, et al., ForceSpinning of polyacrylonitrile for mass production of lithium-ion battery separators, Journal of Applied Polymer Science 133 (1) (2016).
[31] B.C. Weng, et al., The Production of Carbon Nanotube Reinforced Poly(vinyl) Butyral Nanofibers by the Forcespinning (R) Method, Polymer Engineering and Science 55 (1) (2015) 81–87.
[32] V.A. Agubra, et al., Composite Nanofibers as Advanced Materials for Li-ion, Li-O-2 and Li-S Batteries, Electrochimica Acta 192 (2016) 529–550.
[33] V.A. Agubra, et al., Forcespinning: A new method for the mass production of Sn/C composite nanofiber anodes for lithium ion batteries, Solid State Ionics 286 (2016) 72–82.
[34] L. Zuniga, et al., Multichannel hollow structure for improved electrochemical performance of TiO2/Carbon composite nanofibers as anodes for lithium ion batteries, Journal of Alloys and Compounds 686 (2016) 733–743.
[35] N. Obregon, et al., Effect of Polymer Concentration, Rotational Speed, and Solvent Mixture on Fiber Formation Using Forcespinning((R)), Fibers 4 (2) (2016).
[36] J.P. Hooper, Centrifugal Spinneret, in US paptent, U.p Office, USA, 1924 Editor.
[37] B.C. Weng, et al., Fibrous cellulose membrane mass produced via forcespinning (A (R)) for lithium-ion battery separators, Cellulose 22 (2) (2015) 1311–1320.
[38] R.T. Weitz, et al., Polymer nanofibers via nozzle-free centrifugal spinning, Nano Letters 8 (4) (2008) 1187–1191.

[39] X.W. Zhang, Y. Lu, Centrifugal Spinning: An Alternative Approach to Fabricate Nanofibers at High Speed and Low Cost, Polymer Reviews 54 (4) (2014) 677–701.

[40] S. Kim, et al., Phase and microstructural evolution of Sn particles embedded in amorphous carbon nanofibers and their anode properties in Li-ion batteries, Journal of Electroceramics 32 (4) (2014) 261–268.

[41] F. Ahimou, et al., XPS analysis of chemical functions at the surface of Bacillus subtilis, Journal of Colloid and Interface Science 309 (1) (2007) 49–55.

[42] Y. Zhang, L. Jiang, C. Wang, Preparation of a porous Sn@C nanocomposite as a high-performance anode material for lithium-ion batteries, Nanoscale 7 (28) (2015) 11940–11944.

[43] J. Mu, et al., Tin oxide (SnO2) nanoparticles/electrospun carbon nanofibers (CNFs) heterostructures: Controlled fabrication and high capacitive behavior, Journal of Colloid and Interface Science 356 (2) (2011) 706–712.

[44] M.A. Peck, M.A. Langell, Comparison of Nanoscaled and Bulk NiO Structural and Environmental Characteristics by XRD, XAFS, and XPS, Chemistry of Materials 24 (23) (2012) 4483–4490.

[45] N. Zhang, et al., Pitaya-like Sn@C nanocomposites as high-rate and long-life anode for lithium-ion batteries, Nanoscale 6 (5) (2014) 2827–2832.

[46] K.M. Deen, et al., Effect of electrolyte composition on TiO2 nanotubular structure formation and its electrochemical evaluation, Electrochimica Acta 117 (2014) 329–335.

[47] Z. Shen, et al., Tin nanoparticle-loaded porous carbon nanofiber composite anodes for high current lithium-ion batteries, Journal of Power Sources 278 (0) (2015) 660–667.

[48] X. Xia, et al., The effects of electrospinning parameters on coaxial Sn/C nanofibers: Morphology and lithium storage performance, Electrochimica Acta 121 (0) (2014) 345–351.

[49] L. Lang, et al., Hollow Core-Shell Structured Ni-Sn@C Nanoparticles: A Novel Electrocatalyst for the Hydrogen Evolution Reaction, Acs Applied Materials & Interfaces 7 (17) (2015) 9098–9102.

[50] Q. Wang, et al., Uniformly loading NiO nanowalls on graphene and their extremely high capacity and cyclability as anodes of lithium-ion batteries, Materials Letters 118 (2014) 66–68.

[51] L.W. Ji, et al., Recent developments in nanostructured anode materials for rechargeable lithium-ion batteries, Energy & Environmental Science 4 (8) (2011) 2682–2699.

[52] M. Alcoutlabi, et al., Electrospun Nanofibers for Energy Storage, Aatcc Review 11 (6) (2011) 45–51.

[53] H. Zhang, et al., Preparation and electrochemical performance of SnO2@carbon nanotube core–shell structure composites as anode material for lithium-ion batteries, Electrochimica Acta 59 (0) (2012) 160–167.

[54] C.L. Campion, W. Li, B.L. Lucht, Thermal Decomposition of LiPF6-Based Electrolytes for Lithium-Ion Batteries, Journal of the Electrochemical Society 152 (12) (2005) A2327–A2334.

[55] D. Aurbach, M. Moshkovich, A Study of Lithium Deposition-Dissolution Processes in a Few Selected Electrolyte Solutions by Electrochemical Quartz Crystal Microbalance, Journal of the Electrochemical Society 145 (8) (1998) 2629–2639.

[56] L.L. Xing, et al., SnO2/NiO core-shell nanobelts and their high reversible lithium storage capacity arising from synergistic effect, Materials Letters 96 (2013) 158–161.